

MIT Open Access Articles

*Melting and ejecta produced by high velocity
microparticle impacts of steel on tin*

The MIT Faculty has made this article openly available. **Please share**
how this access benefits you. Your story matters.

Citation: Lienhard, Jasper, Veyssset, David, Nelson, Keith A and Schuh, Christopher A. 2021.
"Melting and ejecta produced by high velocity microparticle impacts of steel on tin." Journal of
Applied Mechanics, 88 (11).

As Published: 10.1115/1.4051593

Publisher: ASME International

Persistent URL: <https://hdl.handle.net/1721.1/141165>

Version: Final published version: final published article, as it appeared in a journal, conference
proceedings, or other formally published context

Terms of Use: Article is made available in accordance with the publisher's policy and may be
subject to US copyright law. Please refer to the publisher's site for terms of use.



Jasper Lienhard

Department of Materials Science and Engineering,
MIT,
Cambridge, MA 02139
e-mail: jzl@mit.edu

David Veyssset¹

Institute for Soldier Nanotechnologies,
MIT,
Cambridge, MA 02139
e-mail: dveyssset@mit.edu

Keith A. Nelson

Institute for Soldier Nanotechnologies,
Department of Chemistry,
MIT,
Cambridge, MA 02139
e-mail: kanelson@mit.edu

Christopher A. Schuh²

Department of Materials Science and Engineering,
MIT,
Cambridge, MA 02139
e-mail: schuh@mit.edu

Melting and Ejecta Produced by High Velocity Microparticle Impacts of Steel on Tin

At sufficiently high velocities, a microparticle impacting a metal substrate can cause ejection of material from the substrate and impact-induced melting, both of which can result in erosion. Here, we directly image the impact of individual hard steel microparticles on soft tin substrates, at controlled impact velocities in the range of ~ 100 to 1000 m/s. By using scanning electron and laser scanning confocal microscopy, we characterize the surface morphology, depth, and volume of each impact crater. We observe a gradual onset of impact-induced melting in the craters, as well as the production of increasing amounts of ejecta from the target metal. By comparing measurements of impact and rebound velocity to an elastic-plastic model, we observe that at a high enough impact velocity, melting and ejection begin to consume additional kinetic energy beyond that expected by plastic deformation of the target material alone. By calculating the excess energy dissipation using this elastic-plastic model, we show that although this divergent behavior is associated with the onset of melting, the majority of the ejected volume must be solid rather than liquid.
[DOI: 10.1115/1.4051593]

Keywords: high velocity impact, micromechanics, erosion, ejecta, melting, cratering, impact, plasticity

Introduction

High velocity impacts can induce cratering and erosion processes important to numerous fields of study, such as micrometeoroid damage on spacecraft [1,2], asteroid collisions with planets [3,4], erosion of pipeline interiors by solid particle streams [5,6], and sand erosion of turbine blades [7]. Many previous studies have examined impact mechanics and impact-induced erosion, often by either studying the erosive effects of a stream of particles hitting a surface [8–10] or by conducting post-mortem examination of individual craters created by the impact of a single solid object [11,12]. Complex material behavior induced by high velocity impact has been observed at many scales and across many impact scenarios and includes the excavation of craters [13], launch of ejecta clouds [14–16], hydrodynamic shock-induced jetting [17–19], and chemical reactions at impact sites [20]. Furthermore, several mechanisms of erosion by which material is removed from a surface during impact have been documented for different materials and at varying impact speeds and angles of incidence. These include cutting and ploughing [21,22], microforging and breaking of extruded crater lips [23–25], and ejection of melted material [26].

In recent years, the development of a laser-induced particle impact test (LIPIT) has enabled high-resolution in situ imaging of single microparticle impacts across a range of controlled impact velocities [27–29]. By imaging the interaction between an impacting spherical particle and a substrate with nanosecond-level resolution, accurate measurements of impact and rebound velocity are possible, as well as direct in situ observation of impact-induced material behavior including jetting, adhesion, fragmentation, melting, and hydrodynamic penetration [29–33]. An assortment of particle impactor and target substrate materials have been tested with LIPIT, including metals, ceramics, polymers, and many combinations thereof [34–37]. Recent work by Hassani-

Gangaraj et al. used LIPIT to study the impact of tin particles on a tin substrate and observed that above a certain impact velocity, single particle impacts caused erosion of the substrate by a mechanism of ejection of fragmented and melted material [26]. In the present work, we similarly use LIPIT to study cratering and erosion processes, examining melt and ejecta created by the impact of single microparticles against a ductile metal substrate at normal incidence. In particular, we use strong spherical stainless-steel particles to impact a relatively soft high purity tin substrate, allowing us to restrict plastic deformation and melting to the substrate material only and enabling quantification of material ejected from the substrate during impact.

An advantage of using essentially rigid impactors on soft substrates is that the plastic response is expected to follow a known power law scaling between the coefficient of restitution (i.e., the ratio of the particle's rebound velocity to the impact velocity) and the impact velocity. Departures from that scaling then permit quantitative analysis of the onset of new physical phenomena. For example, Sun et al. used LIPIT to examine spherical microparticle impacts of copper and, for some particle–substrate material pairings, identified a critical “divergence velocity,” where the plasticity power law failed to capture the energy dissipation seen [38]. In the case of copper impacting copper, Sun et al. attributed this divergence to the onset of hydrodynamic jetting. In the present work on tin, we use a similar approach to quantify the onset of melting.

Materials and Methods

A 3.2 mm thick, 99.85% tin plate obtained from Alfa Aesar (Ward Hill, MA) was cut into 15×15 mm squares using a band saw for use as substrates in these experiments. One side of each tin substrate was ground and polished using standard metallographic preparation techniques to a final $0.02 \mu\text{m}$ colloidal silica mirror finish. After the tin substrate had been polished, the grain boundaries were visible under an optical microscope, and the average grain size of the tin was several hundred micrometers; this is far larger than the scale of the experiments, so each experiment essentially samples a single crystal (of unknown orientation). 304 stainless-steel particles manufactured by Cospheric (Santa

¹Present address: Hansen Experimental Physics Laboratory, Stanford University, Stanford, CA 94305.

²Corresponding author.

Contributed by the Applied Mechanics Division of ASME for publication in the JOURNAL OF APPLIED MECHANICS. Manuscript received April 12, 2021; final manuscript received June 19, 2021; published online July 20, 2021. Assoc. Editor: Yong Zhu.

Barbara, CA), each selected to have a diameter of $12.5 \pm 0.5 \mu\text{m}$, were used as impactors. Figure 1 shows a scanning electron micrograph of a stainless-steel particle representative of those used in this study, possessing near-perfect sphericity and a diameter of approximately $12 \mu\text{m}$. All of the particles we used were highly spherical and had a mostly smooth surface morphology. Some particle surfaces had patches of a fine wave-like morphology characteristic of the solidification process used in their manufacture, as shown in Fig. 1.

Thirty-eight single particle impact tests were conducted at impact velocities ranging from 117 to 1020 m/s using a custom-built micro-ballistic optical platform. This platform, which we refer to as the LIPIT, uses a laser pulse (Nd-YAG, 532-nm wavelength, 10 ns duration) to launch individual microparticles from a three-layered launch pad consisting of a $210 \mu\text{m}$ glass substrate, a 60 nm gold layer, and a $30 \mu\text{m}$ polyurea film on top. Before impact, particles are spread finely across the top of the launch pad with a lens cleaning paper. For each shot, a single, isolated particle on the launch pad with the desired diameter is selected for launch using a camera. The 532 nm wavelength laser then ablates the gold film of the launch pad, causing the polyurea layer to expand rapidly and eject the selected particle. A second laser pulse (640 nm wavelength, $30 \mu\text{s}$ duration) is used to illuminate the field of view for imaging by a separate ultra-high-speed camera (Specialised Imaging, SIMX 16). This camera collects multiframe sequences of each impact event with a 5-ns exposure time and an adjustable interframe time, which can then be used to extract the impact and rebound velocities (v_i and v_r , respectively) with a $\pm 2\%$ uncertainty. Each steel particle impacts normal to the tin substrate within ± 3 deg.

After the impact tests were completed, each impact site on the tin substrate was examined in a Zeiss Merlin scanning electron microscope (SEM), which was also used to produce the image in Fig. 1 of the as-received impactor particle. In addition, optical surface profilometry was conducted at each impact site using a laser scanning confocal microscope (VK-X200, Keyence).

Results

Table 1 reports the impact velocity (v_i) and the rebound velocity (v_r) for each impact test. Also listed are the measured diameter of each particle before launch and the depth and volume of each crater created upon impact, measured with the confocal microscope.

The coefficient of restitution (v_r/v_i) is plotted as a function of impact velocity for all impact tests in Fig. 2. All but one of the particles rebounded from the substrate upon impact. The one impactor particle that failed to rebound and remained embedded in the substrate occurred at one of the highest impact speeds tested, 955 m/s.

Figure 3 shows post-mortem scanning electron micrographs of 16 representative impact craters across a range of velocities,

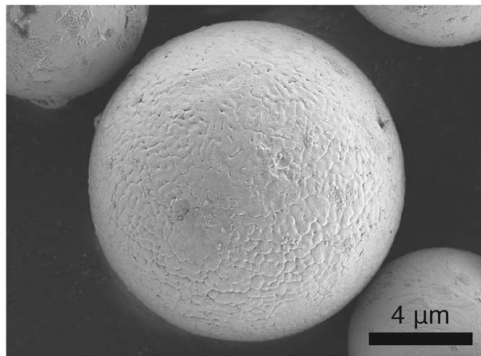


Fig. 1 An SEM image of a stainless-steel particle representative of those used in as impactors in this study, with a diameter of $12 \mu\text{m}$

Table 1 Impact velocity, rebound velocity, particle diameter, crater depth, and volume of each impact crater

V_i (m/s)	V_r (m/s)	Diameter (μm)	Crater depth (μm)	Crater volume (μm^3)
117 \pm 2	21 \pm 0.4	12.9 \pm 0.2	1.24 \pm 0.05	30 \pm 2
134 \pm 3	21 \pm 0.4	12.9 \pm 0.2	1.52 \pm 0.05	27 \pm 2
140 \pm 3	22 \pm 0.4	12.6 \pm 0.2	1.43 \pm 0.06	36 \pm 2
147 \pm 3	21 \pm 0.4	12.9 \pm 0.2	1.22 \pm 0.07	35 \pm 1
163 \pm 3	22 \pm 0.4	12.9 \pm 0.2	1.41 \pm 0.07	39 \pm 2
165 \pm 3	25 \pm 0.5	12.9 \pm 0.2	1.33 \pm 0.07	40 \pm 2
189 \pm 4	22 \pm 0.4	12.2 \pm 0.2	1.62 \pm 0.1	47 \pm 1
196 \pm 4	22 \pm 0.4	12.6 \pm 0.2	1.59 \pm 0.22	58 \pm 1
197 \pm 4	25 \pm 0.5	12.2 \pm 0.2	1.79 \pm 0.11	49 \pm 3
203 \pm 4	28 \pm 0.6	12.2 \pm 0.2	1.98 \pm 0.11	78 \pm 4
230 \pm 5	25 \pm 0.5	12.6 \pm 0.2	2.08 \pm 0.13	69 \pm 2
282 \pm 6	29 \pm 0.6	12.2 \pm 0.2	2.56 \pm 0.02	132 \pm 3
310 \pm 6	30 \pm 0.6	12.6 \pm 0.2	3.19 \pm 0.02	180 \pm 4
348 \pm 7	33 \pm 0.7	11.9 \pm 0.2	3.02 \pm 0.12	164 \pm 7
360 \pm 7	38 \pm 0.8	12.2 \pm 0.2	3.21 \pm 0.05	189 \pm 7
364 \pm 7	31 \pm 0.6	12.2 \pm 0.2	3.53 \pm 0.01	219 \pm 5
400 \pm 8	30 \pm 0.6	12.9 \pm 0.2	4.16 \pm 0.03	331 \pm 8
404 \pm 8	29 \pm 0.6	11.9 \pm 0.2	3.4 \pm 0.01	168 \pm 3
422 \pm 8	35 \pm 0.7	12.2 \pm 0.2	3.31 \pm 0.01	306 \pm 8
460 \pm 9	34 \pm 0.7	11.9 \pm 0.2	4.39 \pm 0.23	221 \pm 4
476 \pm 10	33 \pm 0.7	12.6 \pm 0.2	4.28 \pm 0.03	345 \pm 6
482 \pm 10	36 \pm 0.7	11.9 \pm 0.2	5.43 \pm 0.1	410 \pm 7
498 \pm 10	29 \pm 0.6	12.6 \pm 0.2	5.49 \pm 0.03	490 \pm 9
548 \pm 11	29 \pm 0.6	11.9 \pm 0.2	5.82 \pm 0.16	400 \pm 7
571 \pm 11	22 \pm 0.4	12.2 \pm 0.2	5.49 \pm 0.05	482 \pm 7
578 \pm 12	20 \pm 0.4	11.9 \pm 0.2	5.33 \pm 0.07	475 \pm 10
638 \pm 13	24 \pm 0.5	12.2 \pm 0.2	6.04 \pm 0.02	573 \pm 10
655 \pm 13	26 \pm 0.5	11.9 \pm 0.2	6.68 \pm 0.06	580 \pm 10
658 \pm 13	16 \pm 0.3	11.9 \pm 0.2	6.6 \pm 0.73	451 \pm 8
719 \pm 14	22 \pm 0.4	12.2 \pm 0.2	6.8 \pm 0.5	704 \pm 10
740 \pm 14	19 \pm 0.4	11.9 \pm 0.2	8.69 \pm 0.4	848 \pm 15
810 \pm 16	22 \pm 0.4	12.2 \pm 0.2	9.01 \pm 0.8	986 \pm 25
902 \pm 18	15 \pm 0.3	12.2 \pm 0.2	10.88 \pm 1	1064 \pm 27
921 \pm 18	11 \pm 0.2	12.2 \pm 0.2	12.9 \pm 0.8	953 \pm 19
929 \pm 19	12 \pm 0.2	12.6 \pm 0.2	16.1 \pm 1.4	1103 \pm 58
955 \pm 19	0	11.2 \pm 0.2	N/A	N/A
956 \pm 19	20 \pm 0.4	13.3 \pm 0.2	12 \pm 0.8	1498 \pm 60
1020 \pm 20	20 \pm 0.4	13.3 \pm 0.2	8.64 \pm 1.1	992 \pm 55

demonstrating the progression in crater size and substrate melting as impact velocity is increased. At the lowest impact speeds, there is no evidence of melting in any of the craters. The lowest speed to demonstrate evidence that substrate melting had occurred during impact is 310 m/s, where a small area at the top of the

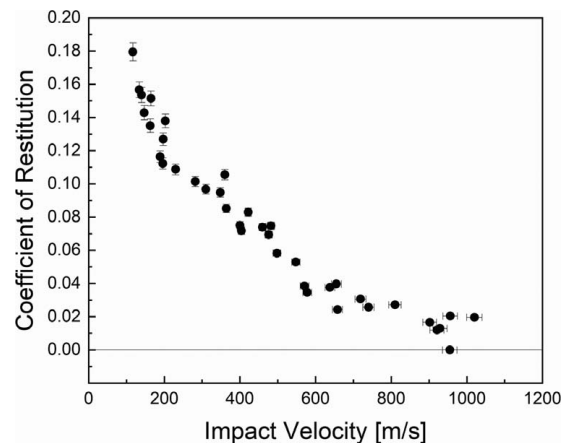


Fig. 2 Coefficient of restitution, the ratio of rebound velocity to impact velocity, is plotted as a function of impact velocity. One particle impacting at 955 m/s did not rebound, as indicated by the lone zero coefficient of restitution value.

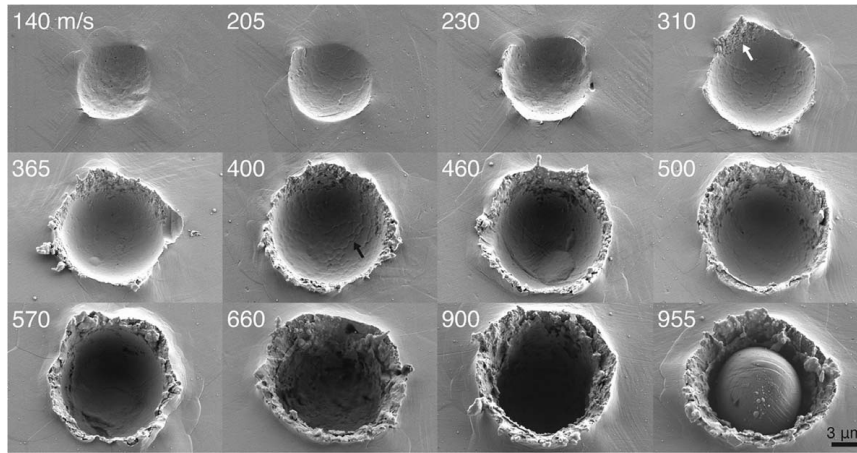


Fig. 3 Sixteen representative impact craters across a wide range of impact velocities. The highest velocity shown in this figure, 955 m/s, is the lone impact test for which the particle did not rebound upon impact and instead remained embedded in its crater. Images were taken at a 15 deg angle.

crater rim has a smoothed bubble-like surface characteristic of melted and resolidified metal. This is denoted with a white arrow in Fig. 3. This type of melted and solidified surface becomes more prominent at higher velocities, and around 400 m/s, it extends around the entire outer rim of the crater. As impact velocity is increased further, evidence of melted and resolidified material extends inward from the crater rim and down into the crater. By 660 m/s, the characteristic resolidified structure covers the entire surface of the crater impact site.

Several lower velocity craters, such as the one denoted with a black arrow at 400 m/s, display a wavy texture inside the crater similar to that seen on the surface of the impactor particles before launch in Fig. 1. These features are interpreted as imprints of the rigid steel particle impactor surface morphology on the crater and are not related to melting of the tin during impact. The bottom right impact, at 955 m/s, shows the single case where the stainless-steel particle lodged into the crater. The steel particle, which is much stronger than the tin substrate, appears generally undeformed and spherical although the faint lines visible on the surface of the particle could be slip traces produced by plastic deformation.

Figure 4 shows 13-frame sequences of the moment of impact and particle rebound at four speeds: 140, 460, 660, and 920 m/s. At the higher impact speeds, we observe material ejection from the substrate occurring at the moment of impact. This can be seen in the fourth frame of Figs. 4(b)–4(d) and is indicated by white arrows. At the highest speed shown here, 920 m/s, Fig. 4(d), material ejection continues for hundreds of nanoseconds after the initial instant of impact and the particle only begins to reemerge from the surface at least 500 ns after initial impact. Ejecta clouds can be tracked across multiple frames, as indicated by the white circle in the eighth frame of Fig. 4(d).

In Fig. 5, we show the progression of increasing amounts of melted and resolidified material as impact velocity is increased by showing SEM images of three impact craters taken at a steep angle. At 460 m/s, it can be seen that a ring of melted and resolidified material wraps around the perimeter of the crater. At 500 m/s, this melted and solidified morphology extends further down the walls of the crater and at 740 m/s covers the entire inner surface of the impact crater.

Figure 6(a) shows a representative crater image taken with the laser scanning confocal microscope of an impact at one of the higher speeds tested, 900 m/s. A cross-sectional profile of this same crater based on the data in Fig. 6(a) is shown in Fig. 6(b). The area highlighted in red in Fig. 6(b) shows that a significant amount of material becomes piled up around the rim of the crater. The volume of the crater itself is highlighted in blue and is defined as all empty volume below the horizontal plane. Figure 6(c) shows

the maximum depth, or the vertical distance from the deepest point of each crater to the horizontal surface plane, of all craters except the one impact where the particle did not rebound. The depth increases fairly linearly with impact velocity, with larger scatter and uncertainty in the measurements at the highest impact velocities due to slightly more uneven bottom surfaces at higher velocities.

In Fig. 6(d), we calculate and plot the total substrate material lost to ejection at each point. As the tin substrate material is incompressible and mass is conserved, the net volume of material lost (V_{jec}) is equal to the measured pile-up volume of each crater subtracted from the measured crater volume. It can be seen that at the lowest speeds, no volume is lost from the substrate, and that starting at around 300 m/s, volume starts to be lost to ejection. The highest two impact velocities shown, 956 and 1020 m/s, have lost volumes of 964 and 733 μm^3 , respectively. The lost volume measurements correlate closely with the in situ imaging observations (Fig. 4), where no volume is seen ejected at the lowest speeds, and significant ejection occurs at the highest speeds.

Discussion

We believe the observed melting in these experiments is primarily caused by the adiabatic heat of plastic deformation rather than the propagation of high-pressure shock waves through the substrate upon impact. To verify this, we can estimate an upper bound of the pressure P at the shock front that propagates into the substrate at the moment of impact using the equation $P = (1/2)\rho v_s v_i$, where ρ is the density of the particle and v_s is the velocity of the shock front in the substrate. An expression for the velocity of the shock front can be obtained from the shock Hugoniot equation of state, an experimentally determined relation that describes the shock response of a material not undergoing a phase transition, $v_s = c_0 + (1/2)s v_i$, where s is an empirical material-specific parameter and c_0 is the bulk sound velocity in the material at zero pressure. For tin, $s = 1.49$ and $c_0 = 3320$ m/s [39]. The density provided by the manufacturer of the stainless-steel particles we used is 7719.6 kg/m³. At the lowest impact velocity tested (117 m/s), this gives a pressure of 1.5 GPa, and at the highest velocity (1020 m/s), a pressure of 16.1 GPa. According to the shock Hugoniot and melting curve data in Refs. [40,41], it is unlikely that melting would occur at these pressures, and a pressure of about 50 GPa, or a velocity of about 2500 m/s, would be required to achieve melting on the basis of the initial shock itself. It is possible that partial melting upon shock release could occur; however, it has been reported that this would require an initial shock of roughly 22 GPa, also significantly higher than that achieved in our experiments [42].

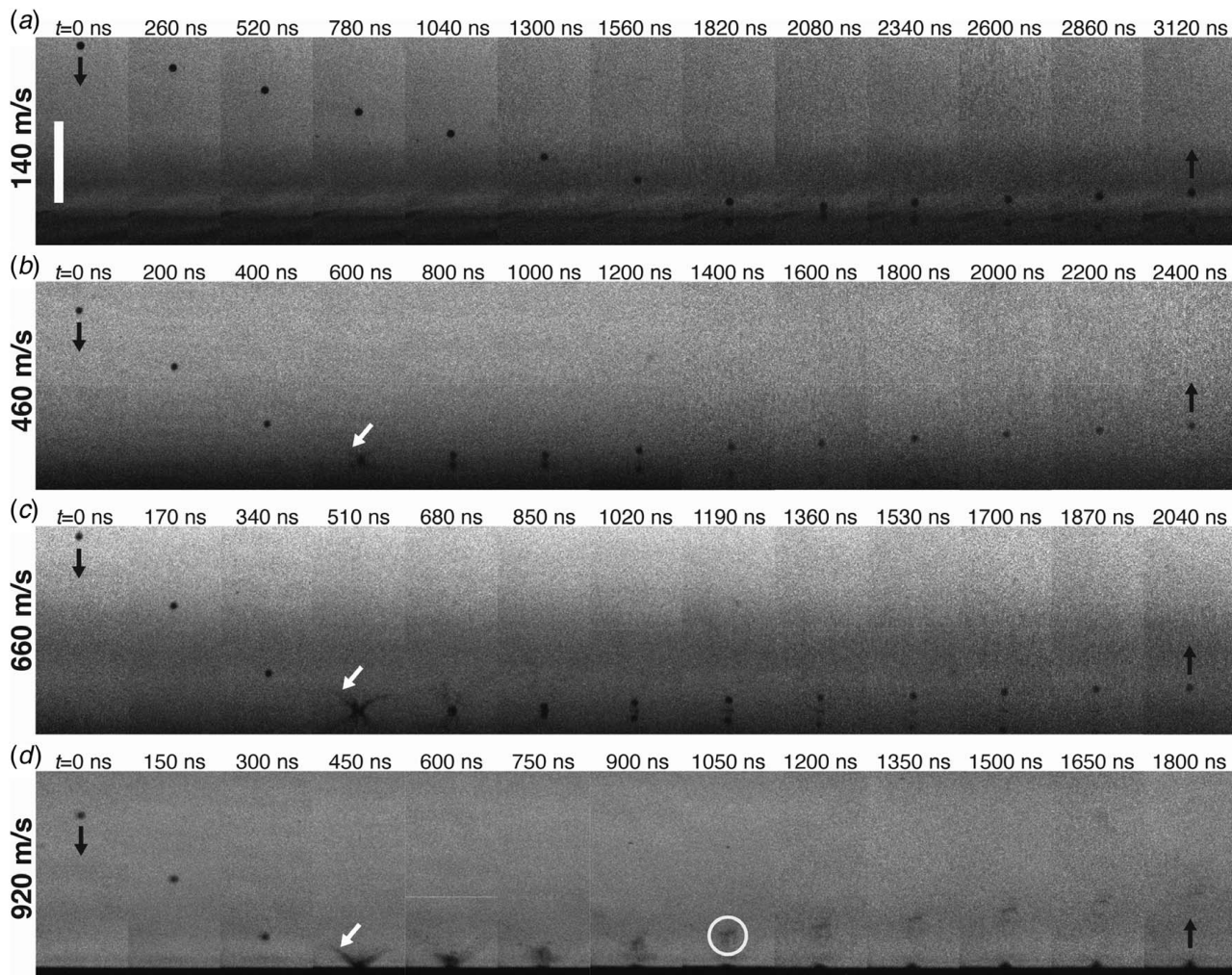


Fig. 4 Frame-by-frame in situ impact images, each with a 5 ns exposure time, at four different impact velocities: (a) 140 m/s, (b) 460 m/s, (c) 660 m/s, and (d) 920 m/s. At the lowest speed shown, 140 m/s, no material ejection is observed during impact. At each of the three higher speeds shown, substrate material is ejected during the impact, indicated by the white arrows. At higher speeds, ejecta clouds can be tracked across multiple frames, as indicated by the white circle in (d). Scale bar is 200 μm .

In their article examining tin microparticle impacts on tin substrates, Hassani-Gangaraj et al. used a simple thermodynamic balance of kinetic and thermal energy from plasticity to predict the impact velocity at which substrate melting begins [26]. This model assumes that upon impact, some fraction of the particle's kinetic energy, α , will be imparted to the substrate as plasticity. In addition, some fraction of that kinetic energy, β , will be dissipated as heat during plastic deformation. They then balanced this fraction of particle kinetic energy dissipated as heat in the substrate

with the energy required to melt a relevant affected volume of substrate material:

$$\frac{\beta\alpha}{2} m_p v_i^2 = \rho_{\text{sub}} V_{\text{aff}} [c_p (T_m - T_o) + H_f] \quad (1)$$

In this equation, m_p is the mass of the particle, V_{aff} is the relevant affected volume in which temperature increases upon impact, and ρ_{sub} , c_p , T_m , and H_f are the density, heat capacity, melting

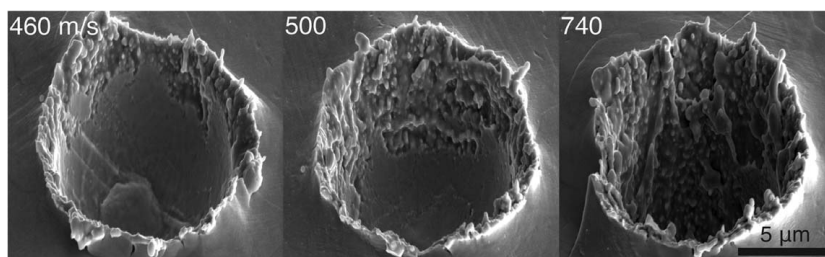


Fig. 5 SEM images of three craters taken at 460, 500, and 740 m/s. Images were taken at a 40 deg angle to allow for imaging of the walls and bottom of each crater, revealing the increasing amount of melted material in this velocity range.

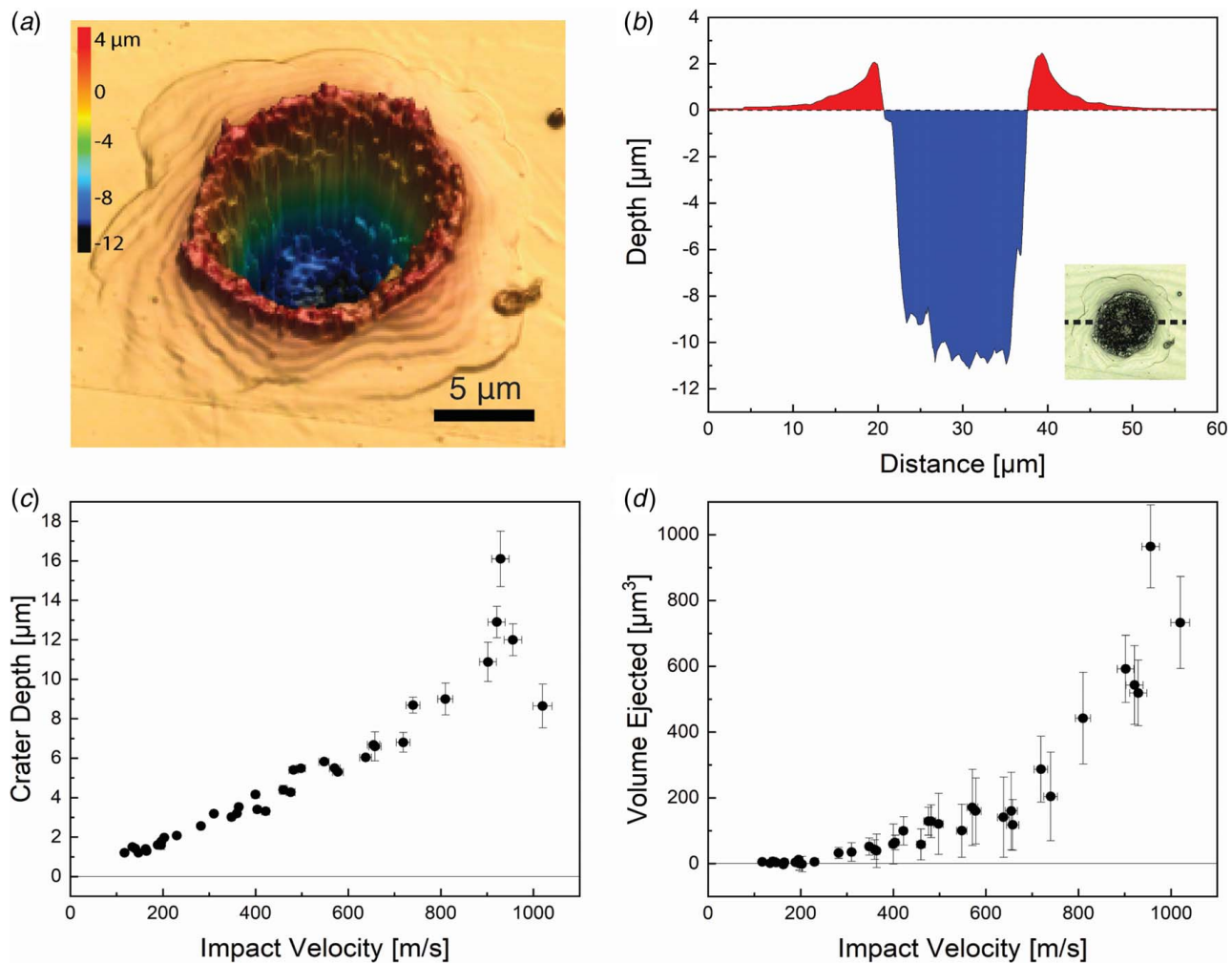


Fig. 6 Surface profilometry of each impact site: (a) laser confocal image of the impact area for the impact that occurred at 900 m/s, (b) an example cross-sectional surface profile, taken on the impact that occurred at 900 m/s, with the piled-up volume shaded above the horizontal plane and the crater volume shaded separately below the horizontal plane, (c) maximum depth measurements of each impact site, and (d) volume ejected from each impact site, calculated as the difference between the crater volume and the pile-up volume

temperature, and enthalpy of fusion of the substrate material, respectively. The affected volume, V_{aff} , is estimated as the product of the contact area of the particle with the substrate and the depth of thermal penetration or the characteristic distance for heat conduction $\sqrt{kt/\rho_{sub}c_p}$, where k is the thermal conductivity of the substrate and t is the contact time of the particle before rebound which can be estimated using a dimensional analysis as the particle diameter divided by the impact velocity. Contact time can also be estimated directly from the frame-by-frame in situ images, and we find good agreement between these two approaches.

We introduce the appropriate material properties for tin ($\rho_{sub} = 7265 \text{ kg/m}^3$, $c_p = 228 \text{ J/kg-K}$, $T_m = 231.9^\circ\text{C}$, and $H_f = 60.2 \text{ J/g}$) and an estimated median value for $\beta = 0.6$ [43–45]. To capture our typical results, we use an average particle diameter of 12.5 μm and an average measured contact area of 200 μm^2 , and note that $\alpha \sim 1 - (v_r/v_i)^2$ is very close to unity for all of our experiments here where steel does not absorb energy by deforming and can be approximated as an elastic impactor. With these values, we solve Eq. (1) for v_i and obtain a value of $\sim 300 \text{ m/s}$. This is rather close to the observed gradual onset of melting that begins at about 310 m/s and increases significantly as the impact velocity increases further. As a first-order approximation, this is an encouraging validation that plasticity and its associated adiabatic heating underlie melting in these experiments. In what follows, we proceed to conduct a more nuanced analysis along those lines.

Several theoretical and empirical models have been proposed to predict the plastic energy dissipation and rebound behavior during the impact of a sphere with a substrate [46–52], and here, we employ a semi-empirical plasticity model proposed by Wu et al. to analyze our impact data [47,48]. By using finite element simulations, Wu et al. showed that for an elastic impactor and elastic-perfectly plastic substrates, the coefficient of restitution decreases in proportion to $v_i^{-1/2}$:

$$\text{CoR} = \frac{v_r}{v_i} = 0.78 \left(\frac{v_y E^*}{v_i Y_d} \right)^{\frac{1}{2}} \quad (2)$$

where Y_d is a dynamic yield strength of the substrate material, and the reduced modulus of the particle and substrate materials, E^* , is defined as follows:

$$\frac{1}{E^*} = \frac{1 - \nu_1^2}{E_1} + \frac{1 - \nu_2^2}{E_2} \quad (3)$$

where the subscripts 1 and 2 refer to properties of particle and substrate, respectively, including the Young's modulus E and Poisson's ratio ν . The velocity at which plastic deformation begins, v_y , has been defined by Johnson [52] as follows:

$$v_y = \left(\frac{26Y_d^5}{\rho E^{*4}} \right)^{\frac{1}{2}} \quad (4)$$

where ρ is the density of the impacting particle.

It is important to note that our tin substrate is not a true elastic-perfectly plastic material as assumed by this model; for our velocities, strain hardening, strain-rate hardening, and adiabatic heating certainly all occur. The analysis of our data with Eq. (2) therefore approximates the material's dynamic yield strength, Y_d , as a single "effective" value, which averages over all the temperatures, strains, and strain rates that occur during the impact, as done by, e.g., Sun et al. for Cu [38].

In Fig. 7, we replot the same coefficient of restitution data presented in Fig. 2 on log-log scales. It can be seen that all points up to the range of about 400 to 500 m/s fit reasonably well to the scaling law of Eq. (2), with the coefficient of restitution decreasing proportionally to $v_i^{-1/2}$. This is shown by the solid regression line with a slope of $-1/2$. Using this regression line of all points up to and including the point at 476 m/s, Eq. (2) can be solved to obtain a dynamic yield strength for the tin substrate of $Y_d = 225$ MPa.

As the impact velocity increases beyond around 450 m/s, a transition from the plasticity behavior predicted by Eq. (2) begins to occur, and the coefficient of restitution decreases with a much steeper slope, approximately proportional to v_i^{-2} . For clarity, points above this divergence velocity are shaded in red in Fig. 7 and a second dashed regression line is shown with a slope of -2 . As impact velocity continues to increase, the coefficient of restitution measurements become increasingly distant from the simple elastic-plastic impact mechanics described by Eq. (2). One possible explanation for this change in behavior is that a change in plasticity begins to occur around 400–500 m/s, such as a transition from a fully plastic to a deeply plastic behavior as described by Yildirim et al. [50]. In the work of Yildirim et al., as well as work by Hassani et al. [53], a transition from a slope of $v_i^{-1/2}$ to approximately v_i^{-1} has been observed in several metals and attributed to a shift in rebound plasticity behavior with the initiating location of rebound moving into the substrate. However, no reports that we are aware of have observed such a sharp divergence from $v_i^{-1/2}$ to a steeper slope of v_i^{-2} that is then sustained across several hundreds of meters per second. While we cannot rule out a change in

plasticity behavior contributing to the divergence in the present case, it is likely that the loss of kinetic energy to other mechanisms beyond dissipation by plastic deformation of the substrate is occurring. In particular, we believe that the combination of melting and substrate material ejection is primarily responsible for the present divergence. This is supported by the clear shift in impact behavior shown in Fig. 4, and the unambiguous rise of melting prominence in SEM images of Figs. 3 and 5; melting and ejection are clearly occurring over the range of velocities associated with the power law divergence, and it seems reasonable to pursue an analysis that attributes the latter directly to the former. As we shall see below, the emergence of melting and the formation of ejecta are more than sufficient to explain the magnitude of the divergence here.

To quantitatively determine the excess energy lost in each impact beyond that predicted by Eq. (2), we calculate the rebound kinetic energy (e_r) of each point using the equation:

$$e_r = \frac{m_p v_r^2}{2} \quad (5)$$

The mass of each particle was calculated using diameter measurements of each particle prior to launch (Table 1). The difference between the actual rebound kinetic energy of each impact and the rebound kinetic energy that would be expected were each impact to fall on the Wu et al. power law shown in Fig. 7 is the excess dissipated energy and is plotted in Fig. 8.

The excess dissipated energy in Fig. 8 remains at or close to zero for all the low velocity impacts where the data conform to the Eq. (2) power law. The data begin to deviate significantly from zero in the range of 400–500 m/s and reaches a maximum of ~ 12 nJ at the highest impact speed tested, 1020 m/s. Based on our in situ impact imaging observations shown in Fig. 4 and post-mortem microscopy of each crater site shown in Fig. 3, we propose two possible causes for the divergence behavior. First, it is clear that an increasing amount of tin substrate melts during impact as the velocity increases. The first small hint of melting is visible in the impact crater at 310 m/s, and at 460 m/s, melted and resolidified material forms a continuous ring around the entire circumference of the crater.

If we were to assume that 100% of the excess dissipated energy (Fig. 8) above the divergence velocity went toward melting, we could estimate an upper bound volume of melted material

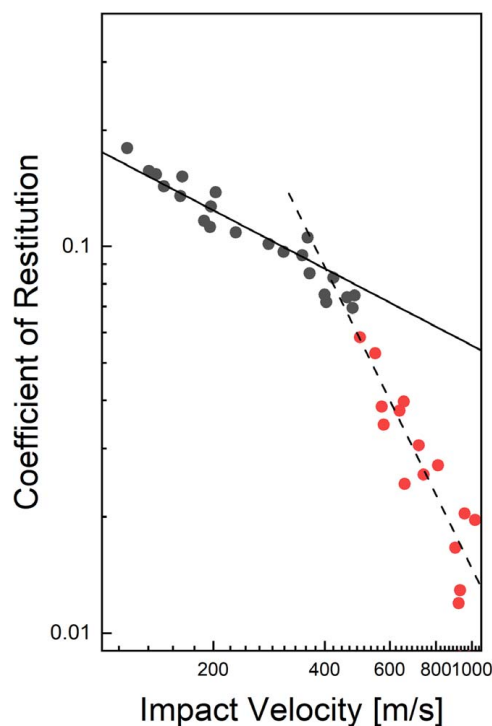


Fig. 7 Coefficient of restitution plotted on log-log scales. The solid line is the best fit of the nondivergent points with a slope of $-1/2$. The divergent points are fitted with a dashed line.

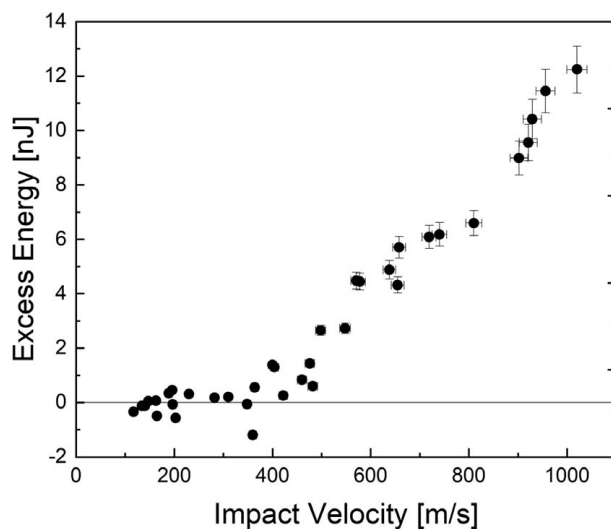


Fig. 8 Excess energy dissipated during impact. Calculated by comparing actual rebound kinetic energy of each impact to the rebound kinetic energy that would occur if each impact fell perfectly on the solid regression line in Fig. 7.

(V_{melt}) using the enthalpy of fusion of tin:

$$e_{melt} = \rho_{sub} V_{melt} H_f \quad (6)$$

In the spirit of this upper bound calculation, Eq. (6) does not include a heat capacity term taking into account temperature rise, since such adiabatic heating effects are already subsumed into our effective dynamic yield strength value, while melting is not. By solving for V_{melt} for each data point in the divergent regime, we obtain the results shown in Fig. 9(a). As can be seen, the maximum possible melt volume from these calculations increases from about $5 \mu\text{m}^3$ at around 500 m/s to about $30 \mu\text{m}^3$ at 1020 m/s. The black arrow in Fig. 9(a) indicates the lowest velocity at which we observed melting in our experiments.

In Fig. 9(b), we plot the same data (gray diamonds) alongside the measurements of net lost or ejected material measured at each impact as shown in Fig. 6(d) (green circles), and the volume of the particle used for each impact (blue triangles). It appears that the melt volumes in the divergent velocity regime are significantly lower than the total amount of lost volume at each impact site, suggesting that a significant portion of the material ejected during impact is solid rather than liquid and by extension that melting is not the largest source of excess energy consumed during impact.

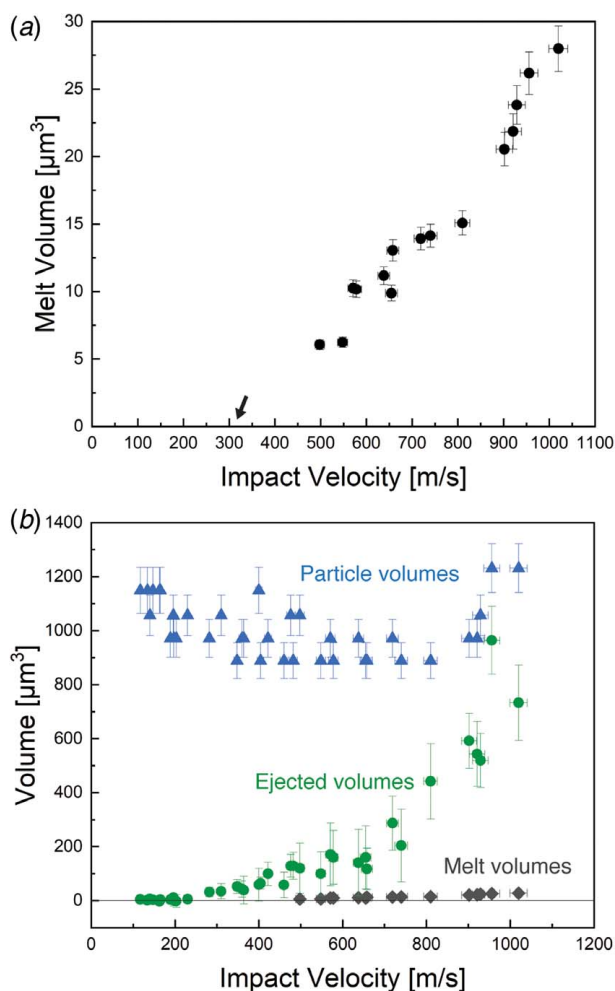


Fig. 9 (a) Calculated melt volumes in the divergent velocity regime if all excess energy goes toward melting substrate material. A black arrow indicates the velocity at which we first observed a small amount of melting. (b) The same data (diamonds) plotted along with the total volume lost or ejected from the substrate measured using confocal microscopy (circles) as well as the volume of the particle used for each impact (triangles).

This is initially a surprising result because the large splashes of ejected matter shown in Fig. 4 are reminiscent of liquid splashes, and the amount of molten and resolidified matter in some of the SEM images of Figs. 3 and 5 seems extensive. At higher speeds, the surface areas of the craters are on the order of $\sim 200 \mu\text{m}^2$ and completely covered with resolidified surface texture. Melt volumes on the order of $\sim 20 \mu\text{m}^3$ as shown in Fig. 9 thus suggest that if the entire contact surface area were melted, the depth of the melted layer on average would be quite thin, perhaps only $\sim 100 \text{ nm}$. Examining the SEM images of the craters in Figs. 3 and 5, for some impacts, this seems plausible, particularly if melted material beads up into larger bubbles seen on the upper walls and rims of the craters in Fig. 5. It is also clear that melting is not evenly distributed across the entire contact surface of each crater, with larger melt volumes at the upper rim, and significantly less prominent melting at the bottom for all speeds.

We now analyze a second obvious source of energy dissipation, namely, the energy required to produce ejecta, rupture it from the substrate and separate individual solid particles, and the kinetic energy that ejecta carries away with it. Starting at around 450 m/s, the in situ impact videos begin to show clear evidence of ejecta clouds in the nanoseconds following the particle–substrate contact. This can be seen, for example, in the impacts at 460, 660, and 920 m/s in Fig. 4. At higher impact velocities, ejecta clouds become increasingly larger. While we cannot directly assess the volume ejected from the video images, our confocal measurements of total net lost volume in Fig. 6(d) allow us to quantify how much substrate material volume is ejected at each impact. Furthermore, in most of our impact videos, any fragments within the ejecta cloud are too small to individually resolve. However, in a couple of videos at the highest impact speeds, we can observe a few distinct larger pieces of ejecta, with diameters of about $1 \mu\text{m}$, comparable to our optical resolution. We therefore assume that the majority of the fragments ejected have a diameter smaller than $1 \mu\text{m}$. For the sake of order-of-magnitude estimations, we further assume that the size and velocity distributions follow a normal distribution. The mean velocity v_{eject} can be measured by tracking the position of localized plumes of ejecta between frames. An example of these plumes can be seen in frames 4–11 of Fig. 4(d) and is marked by a white arrow and white circle in Fig. 4(d). Ejecta velocity measurements for ten impacts in the divergent regime are plotted in Fig. 10(a) as red circles.

Under these assumptions, the total ejecta kinetic energy (e_{ejecta}) can be roughly approximated as follows:

$$e_{ejecta} = \frac{1}{2} m_{eject} v_{eject}^2 = \frac{1}{2} \rho_{sub} V_{eject} v_{eject}^2 \quad (7)$$

where v_{eject} is the average ejecta velocity, and the total mass of ejected material at each impact, m_{eject} , is obtained by multiplying the confocal lost volume (equivalent to ejecta volume V_{eject}) measurements by the density of tin. By using the v_{eject} measurements shown in Fig. 10(a), we calculate kinetic energy carried away by ejecta at ten different velocities in the divergent regime. This is plotted as red circles in Fig. 10(b). Also shown for comparison in Fig. 10(b) are the excess energy calculations from Fig. 8. Although there is a significant error associated with v_{eject} measurements and therefore the calculated e_{ejecta} , overall it can be seen that the kinetic energy of ejecta and the excess energy are certainly of about the same order of magnitude. This verifies that kinetic energy carried away by the ejected solid material could be responsible for a significant portion of the excess energy at higher impact velocities.

Taken together, the aforementioned analyses show that either melting alone or kinetic energy of ejection could easily be sufficient to account for all of the excess energy dissipated for each impact in the divergent regime. However, our data in Fig. 9(b) suggest that less than 10% of the ejected material is likely to be liquid, and it seems that the kinetic energy of ejected material is responsible for a significantly larger share of the

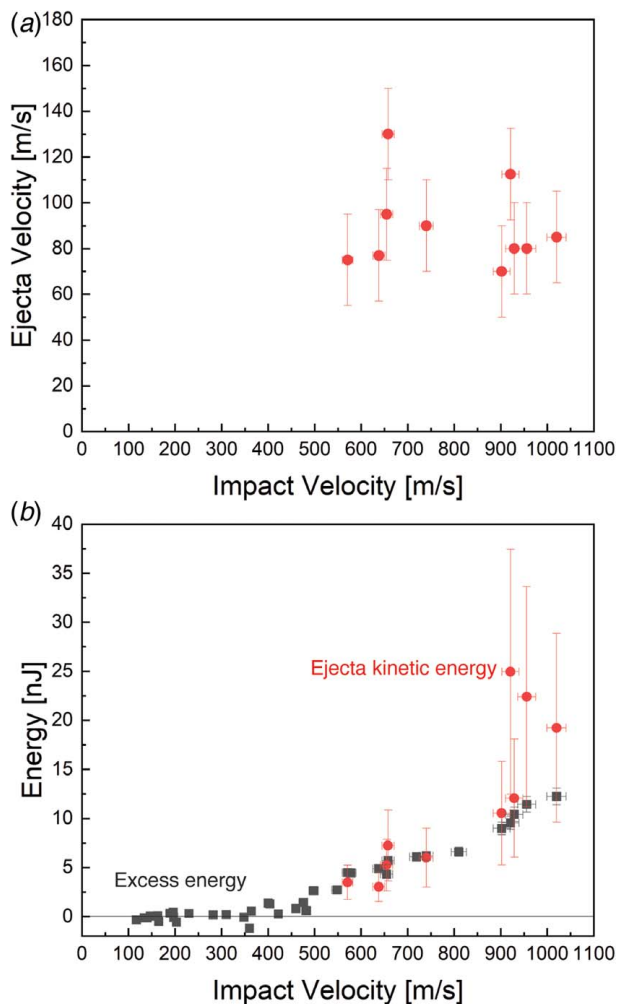


Fig. 10 (a) Direct velocity measurements of the ejecta plumes created during impact for ten of the impacts and (b) kinetic energy associated with the same ten impacts calculated using Eq. (7) (circles), and the total excess energy dissipated during impact data from Fig. 8 (squares)

excess energy than energy contributing to melting. As a topic of future research, we suggest further analysis of this complex interplay among melting, fragmentation, and ejection, and more observations and quantification of ejecta at high speeds.

Conclusion

We conducted velocity-controlled single-particle impacts using a custom-built laser-induced particle impact test. Thirty-eight spherical stainless-steel particles were launched at a tin substrate at normal incidence across a range of velocities from 117 to 1020 m/s. The moment of impact was imaged using a high-speed camera, and the inbound and outbound velocity of each impact was measured directly. Furthermore, the crater produced by each impact on the tin substrate was imaged with both a high-resolution scanning electron microscope and a laser scanning confocal microscope, which allowed for direct measurement of crater depth, crater volume, and volume of pile-up material around each crater's rim. By subtracting the pile-up material at each site from the crater volume, we calculated the net amount of material ejected from the substrate at each impact speed tested.

When comparing our impact and rebound velocity measurements to a model for elastic impacts on an elastic-perfectly plastic target, we find that low velocity impacts (up to a divergence velocity at

around 450 m/s) are well characterized by a single plasticity parameter or effective yield strength. In this range, the coefficient of restitution decreases proportionally to approximately $v_i^{-1/2}$. Above the divergence velocity, however, deviation from the expected behavior occurred with rebound velocity dropping more rapidly than expected. We observed that the onset of divergence correlated closely with the emergence of melting and the significant loss of substrate matter caused by ejection during impact. By calculating an excess divergent energy associated with each impact velocity above the divergence velocity, we calculated an upper bound on substrate melt volumes and found these melt volumes to be much lower than the total amount of ejected volume at each impact site. Furthermore, we also used measurements of ejecta cloud velocities to estimate kinetic energies of ejected material and found these calculations to be reasonably close to the observed excess energy above the divergence velocity.

This analysis leads to two complementary conclusions about energy dissipation by impacts that produce melting. First, the majority of lost kinetic energy in these cases is carried away by ejected material, and second, only a small fraction of the ejected matter is liquid and melting accounts for only a small part of the excess lost energy of the impact.

Acknowledgment

This work was primarily supported by Lawrence Livermore National Laboratory under contract B640614. C.A.S. and K.N. acknowledge the support for collaborative work from US Department of Energy, Office of Science, Office of Basic Energy Sciences, Division of Materials Science and Engineering under Award DE-SC0018091. J.L. also acknowledges Dr. Ievgenia Chaban for her assistance with some of the impact experiments. The authors also acknowledge the following scientists at Lawrence Livermore National Laboratory for their input on this work: Suzanne Ali, Jon Eggert, Kyle Mackay, Brandon Morgan, Fady Najjar, Hye-Sook Park, Jesse Pino, Alison Saunders, and Camelia Stan.

Conflict of Interest

There are no conflicts of interest.

Data Availability Statement

The datasets generated and supporting the findings of this article are obtainable from the corresponding author upon reasonable request.

References

- [1] Bernhard, R. P., Christiansen, E. L., Hyde, J., and Crews, J. L., 1995, "Velocity Impact Damage Into Space Shuttle Surfaces," *Int. J. Impact Eng.*, **17**(1–3), pp. 57–68.
- [2] Christiansen, E. L., Hyde, J. L., and Bernhard, R. P., 2004, "Space Shuttle Debris and Meteoroid Impacts," *Adv. Sp. Res.*, **34**(5), pp. 1097–1103.
- [3] Melosh, H. J., 1984, "Impact Ejection, Spallation, and the Origin of Meteorites," *Icarus*, **59**(2), pp. 234–260.
- [4] Melosh, H. J., and Ivanov, B. A., 1999, "Impact Crater Collapse," *Annu. Rev. Earth Planet. Sci.*, **27**(1), pp. 385–415.
- [5] Parsi, M., Najmi, K., Najafifard, F., Hassani, S., McLaury, B. S., and Shirazi, S. A., 2014, "A Comprehensive Review of Solid Particle Erosion Modeling for Oil and Gas Wells and Pipelines Applications," *J. Nat. Gas Sci. Eng.*, **21**, pp. 850–873.
- [6] Javaheri, V., Porter, D., and Kuokkala, V. T., 2018, "Slurry Erosion of Steel—Review of Tests, Mechanisms and Materials," *Wear*, **408–409**, pp. 248–273.
- [7] Grant, G., and Tabakoff, W., 1975, "Erosion Prediction in Turbomachinery Resulting From Environmental Solid Particles," *J. Aircr.*, **12**(5), pp. 471–478.
- [8] Zu, J. B., Hutchings, I. M., and Burstein, G. T., 1990, "Design of a Slurry Erosion Test Rig," *Wear*, **140**(2), pp. 331–344.
- [9] Stevenson, A. N. J., and Hutchings, I. M., 1995, "Scaling Laws for Particle Velocity in the Gas-Blast Erosion Test," *Wear*, **181–183**, pp. 56–62.
- [10] Wood, R. J. K., Jones, T. F., Ganeshalingam, J., and Miles, N. J., 2004, "Comparison of Predicted and Experimental Erosion Estimates in Slurry Ducts," *Wear*, **256**(9–10), pp. 937–947.

- [11] Poole, L. L., Gonzales, M., French, M. R., Yarberr, W. A., Moustafa, A. R., and Cordero, Z. C., 2020, "Hypervelocity Impact of PrintCast 316L/A356 Composites," *Int. J. Impact Eng.*, **136**.
- [12] Berthoud, L., and Mandeville, J. C., 1997, "Material Damage in Space From Microparticle Impact," *J. Mater. Sci.*, **32**(11), pp. 3043–3048.
- [13] Melosh, H. J., 1989, *Impact Cratering: A Geologic Process*, Oxford University Press, Oxford, UK.
- [14] Johnson, B. C., Bowling, T. J., and Melosh, H. J., 2014, "Jetting During Vertical Impacts of Spherical Projectiles," *Icarus*, **238**, pp. 13–22.
- [15] Housen, K. R., and Holsapple, K. A., 2011, "Ejecta From Impact Craters," *Icarus*, **211**(1), pp. 856–875.
- [16] Kurosawa, K., and Takada, S., 2019, "Impact Cratering Mechanics: A Forward Approach to Predicting Ejecta Velocity Distribution and Transient Crater Radii," *Icarus*, **317**, pp. 135–147.
- [17] Hassani-Gangaraj, M., Veyssset, D., Champagne, V. K., Nelson, K. A., and Schuh, C. A., 2018, "Adiabatic Shear Instability Is Not Necessary for Adhesion in Cold Spray," *Acta Mater.*, **158**, pp. 430–439.
- [18] Tamiyu, A. A., Sun, Y., Nelson, K. A., and Schuh, C. A., 2021, "Site-Specific Study of Jetting, Bonding, and Local Deformation During High-Velocity Metallic Microparticle Impact," *Acta Mater.*, **202**, pp. 159–169.
- [19] Hassani-Gangaraj, M., Veyssset, D., Champagne, V. K., Nelson, K. A., and Schuh, C. A., 2019, "Response to Comment on 'Adiabatic Shear Instability Is Not Necessary for Adhesion in Cold Spray'," *Scr. Mater.*, **162**, pp. 515–519.
- [20] Lee, C., and Kim, J., 2015, "Microstructure of Kinetic Spray Coatings: A Review," *J. Therm. Spray Technol.*, **24**(4), pp. 592–610.
- [21] Finne, I., 1960, "Erosion of Surfaces," *Wear*, **3**(2), pp. 87–103.
- [22] Bitter, J. G. A., 1963, "A Study of Erosion Phenomena Part I," *Wear*, **6**(3), pp. 169–190.
- [23] Sundararajan, G., and Shewmon, P. G., 1983, "A New Model for the Erosion of Metals at Normal Incidence," *Wear*, **84**(2), pp. 237–258.
- [24] Bellman, R., and Levy, A., 1986, "Platelet Mechanism of Erosion of Ductile Metals," *Wear*, **108**, pp. 1–21.
- [25] Hutchings, I. M., 1981, "A Model for the Erosion of Metals by Spherical Particles at Normal Incidence," *Wear*, **70**(3), pp. 269–281.
- [26] Hassani-Gangaraj, M., Veyssset, D., Nelson, K. A., and Schuh, C. A., 2018, "Melt-Driven Erosion in Microparticle Impact," *Nat. Commun.*, **9**(1), pp. 1–7.
- [27] Veyssset, D., Hsieh, A. J., Kooi, S., Maznev, A. A., Masser, K. A., and Nelson, K. A., 2016, "Dynamics of Supersonic Microparticle Impact on Elastomers Revealed by Real-Time Multi-Frame Imaging," *Sci. Rep.*, **6**(1), pp. 1–7.
- [28] Veyssset, David, Lee, Jae-Hwang, Hassani, Mostafa, Kooi, Steven, Thomas, Edwin, and Nelson, Keith, 2021, "High-Velocity Micro-Projectile Impact Testing," *Applied Physics Reviews*, **8**(1).
- [29] Hassani-Gangaraj, M., Veyssset, D., Nelson, K. A., and Schuh, C. A., 2018, "In-Situ Observations of Single Micro-Particle Impact Bonding," *Scr. Mater.*, **145**, pp. 9–13.
- [30] Hassani-Gangaraj, M., Veyssset, D., Nelson, K. A., and Schuh, C. A., 2017, "Melting Can Hinder Impact-Induced Adhesion," *Phys. Rev. Lett.*, **119**(17), pp. 1–5.
- [31] Tamiyu, A. A., and Schuh, C. A., 2020, "Particle Flattening During Cold Spray: Mechanistic Regimes Revealed by Single Particle Impact Tests," *Surf. Coatings Technol.*, **403**.
- [32] Lienhard, J., Crook, C., Azar, M. Z., Hassani, M., Mumm, D. R., Veyssset, D., Apelian, D., Nelson, K. A., Champagne, V., Nardi, A., Schuh, C. A., and Valdevit, L., 2020, "Surface Oxide and Hydroxide Effects on Aluminum Microparticle Impact Bonding," *Acta Mater.*, **197**, pp. 28–39.
- [33] Sun, Y., Veyssset, D., Nelson, K. A., and Schuh, C. A., 2020, "In Situ Observations of Jetting in the Divergent Rebound Regime for High-Velocity Metallic Microparticle Impact," *Appl. Phys. Lett.*, **117**(13).
- [34] Veyssset, D., Hsieh, A. J., Kooi, S. E., and Nelson, K. A., 2017, "Molecular Influence in High-Strain-Rate Microparticle Impact Response of Poly(Urethane Urea) Elastomers," *Polymer*, **123**, pp. 30–38.
- [35] Imbriglio, S. I., Hassani-Gangaraj, M., Veyssset, D., Aghasibeig, M., Gauvin, R., Nelson, K. A., Schuh, C. A., and Chromik, R. R., 2019, "Adhesion Strength of Titanium Particles to Alumina Substrates: A Combined Cold Spray and LIPIT Study," *Surf. Coatings Technol.*, **361**, pp. 403–412.
- [36] Hassani-Gangaraj, M., Veyssset, D., Nelson, K. A., and Schuh, C. A., 2019, "Impact-Bonding With Aluminum, Silver, and Gold Microparticles: Toward Understanding the Role of Native Oxide Layer," *Appl. Surf. Sci.*, **476**, pp. 528–532.
- [37] Hassani, M., Veyssset, D., Nelson, K. A., and Schuh, C. A., 2020, "Material Hardness at Strain Rates Beyond 106 S⁻¹ via High Velocity Microparticle Impact Indentation," *Scr. Mater.*, **177**, pp. 198–202.
- [38] Sun, Y., Veyssset, D., Nelson, K. A., and Schuh, C. A., 2020, "The Transition From Rebound to Bonding in High-Velocity Metallic Microparticle Impacts: Jetting-Associated Power-Law Divergence," *J. Appl. Mech.*, **87**(9).
- [39] Marsh, S. P., 1980, *LASL Shock Hugoniot Data*, Los Alamos Ser. Dyn. Mater. Prop.
- [40] Lazicki, A., Rygg, J. R., Coppari, F., Smith, R., Fratanduono, D., Kraus, R. G., Collins, G. W., Briggs, R., Braun, D. G., Swift, D. C., and Eggert, J. H., 2015, "X-Ray Diffraction of Solid Tin to 1.2 TPa," *Phys. Rev. Lett.*, **115**(7), pp. 1–5.
- [41] Briggs, R., Daisenberger, D., Salamat, A., Garbarino, G., Mezouar, M., Wilson, M., and McMillan, P. F., 2012, "Melting of Sn to 1 Mbar," *J. Phys. Conf. Ser.*, **377**(1).
- [42] Stevens, G. D., Lutz, S. S., Marshall, B. R., Turley, W. D., Veaser, L. R., Furlanetto, M. R., Hixson, R. S., Holtkamp, D. B., Jensen, B. J., Rigg, P. A., and Wilke, M. D., 2008, "Free-Surface Optical Scattering as an Indicator of the Shock-Induced Solid-Liquid Phase Transition in Tin," *J. Appl. Phys.*, **104**(1).
- [43] Ravichandran, G., 2002, "On the Conversion of Plastic Work into Heat During High-Strain-Rate Deformation," *AIP Conference Proceedings*, **620**, pp. 557–562.
- [44] Knysh, P., and Korkolis, Y. P., 2015, "Determination of the Fraction of Plastic Work Converted Into Heat in Metals," *Mech. Mater.*, **86**, pp. 71–80.
- [45] Rittel, D., Zhang, L. H., and Osovski, S., 2017, "The Dependence of the Taylor–Quinney Coefficient on the Dynamic Loading Mode," *Journal of the Mechanics and Physics of Solids*, **107**, pp. 96–114.
- [46] Brach, R. M., Dunn, P. F., and Li, X., 2000, "Experiments and Engineering Models of Microparticle Impact and Deposition," *J. Adhes.*, **74**(1–4), pp. 227–282.
- [47] Wu, C. Y., Yuan, L., and Thornton, C., 2003, "Rebound Behaviour of Spheres for Plastic Impacts," *Int. J. Impact Eng.*, **28**(9), pp. 929–946.
- [48] Wu, C. Y., Li, L. Y., and Thornton, C., 2005, "Energy Dissipation During Normal Impact of Elastic and Elastic-Plastic Spheres," *Int. J. Impact Eng.*, **32**(1–4), pp. 593–604.
- [49] Li, L. Y., Wu, C. Y., and Thornton, C., 2002, "A Theoretical Model for the Contact of Elastoplastic Bodies," *Proc. Inst. Mech. Eng. Part C: J. Mech. Eng. Sci.*, **216**(4), pp. 421–431.
- [50] Yildirim, B., Yang, H., Gouldstone, A., and Müftü, S., 2017, "Rebound Mechanics of Micrometre-Scale, Spherical Particles in High-Velocity Impacts," *Proc. R. Soc. A Math. Phys. Eng. Sci.*, **473**(2204).
- [51] Thornton, C., 1997, "Coefficient of Restitution for Collinear Collisions of Elastic-Perfectly Plastic Spheres," *J. Appl. Mech.*, **64**(2), pp. 383–386.
- [52] Johnson, K. L., *Contact Mechanics*, Cambridge University Press, Cambridge, UK.
- [53] Hassani, M., Veyssset, D., Sun, Y., Nelson, K. A., and Schuh, C. A., 2020, "Microparticle Impact-Bonding Modes for Mismatched Metals: From Co-Deformation to Splating and Penetration," *Acta Mater.*, **199**, pp. 480–494.